

11-14-2008

# Kinetics of Individual Nucleation Events Observed in Nanoscale Vapor-Liquid-Solid Growth

B.J. Kim

*Purdue University - Main Campus*

J Tersoff

*IBM Corp*

S Kodambaka

*IBM Corp*

M.C. Reuter

*IBM Corp*

E A. Stach

*Birck Nanotechnology Center and School of Materials Engineering, Purdue University, eastach@purdue.edu*

*See next page for additional authors*

Follow this and additional works at: <http://docs.lib.purdue.edu/nanopub>



Part of the [Nanoscience and Nanotechnology Commons](#)

Kim, B.J.; Tersoff, J.; Kodambaka, S.; Reuter, M.C.; Stach, E.A.; and Ross, F.M., "Kinetics of Individual Nucleation Events Observed in Nanoscale Vapor-Liquid-Solid Growth" (2008). *Birck and NCN Publications*. Paper 338.  
<http://docs.lib.purdue.edu/nanopub/338>

This document has been made available through Purdue e-Pubs, a service of the Purdue University Libraries. Please contact [epubs@purdue.edu](mailto:epubs@purdue.edu) for additional information.

---

**Authors**

BJ. Kim, J Tersoff, S Kodambaka, M C. Reuter, E A. Stach, and F M. Ross

# Kinetics of Individual Nucleation Events Observed in Nanoscale Vapor-Liquid-Solid Growth

B. J. Kim,<sup>1</sup> J. Tersoff,<sup>2</sup> S. Kodambaka,<sup>2\*</sup> M. C. Reuter,<sup>2</sup> E. A. Stach,<sup>1†</sup> F. M. Ross<sup>2†</sup>

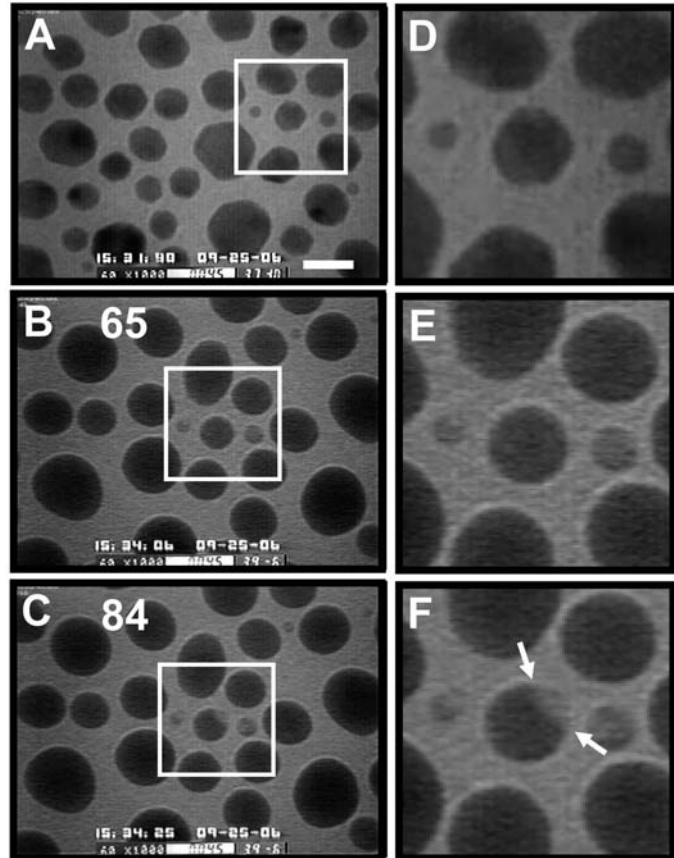
We measured the nucleation and growth kinetics of solid silicon (Si) from liquid gold-silicon (AuSi) catalyst particles as the Si supersaturation increased, which is the first step of the vapor-liquid-solid growth of nanowires. Quantitative measurements agree well with a kinetic model, providing a unified picture of the growth process. Nucleation is heterogeneous, occurring consistently at the edge of the AuSi droplet, yet it is intrinsic and highly reproducible. We studied the critical supersaturation required for nucleation and found no observable size effects, even for systems down to 12 nanometers in diameter. For applications in nanoscale technology, the reproducibility is essential, heterogeneity promises greater control of nucleation, and the absence of strong size effects simplifies process design.

Nucleation is central to all types of growth phenomena, but it is a fleeting event and thus difficult to observe in detail. Phase transitions in macroscopic samples typically involve a large number of distinct nucleation events, and the properties of the final material (such as grain-size distribution) are determined by the statistical ensemble of nucleation events. However, systems that are sufficiently small will transform by a single nucleation event. This raises issues such as statistical variability and size effects (1–3). These classic issues take on new urgency in the context of nanoscale technology, in which an entire functional structure such as a nanowire transistor may depend on a single nucleation event. Only recently, using innovative microscopy techniques, has it become feasible to study individual nucleation events in nanoscale systems (4–10).

We used ultrahigh-vacuum transmission electron microscopy (UHV-TEM) to examine the growth of Si from a AuSi eutectic liquid, a system of particular relevance for the initial stages of nanowire growth by the vapor-liquid-solid process (VLS) (11) and one in which devices such as wrap-gate field-effect transistors have been demonstrated (12–14). By comparing quantitative measurements of nucleation and growth with a simple kinetic model, we determined the critical supersaturation of Si in AuSi required for nucleation and explained in detail the subsequent growth kinetics. Hofmann *et al.* (10) recently reported in situ observations of nucleation and growth in a similar system, addressing the

“incubation time” for nucleation, which primarily reflects the vapor-liquid kinetics and is not sensitive to the nucleation process. Here, we have extracted key information about the nucleation process itself, which allows us to examine size effects and reproducibility, both of which are important for a fundamental understanding of nucleation and for reliable fabrication of nanowires for applications.

**Fig. 1.** (A to C) Bright-field images extracted from a video obtained during nucleation of Si from polycrystalline Au clusters at 525°C and  $4 \times 10^{-6}$  torr disilane. Scale bar, 20 nm. (A) Image acquired before opening the leak valve, showing polycrystalline Au particles, as indicated by their faceted shapes and by the interparticle variations in their bright-field contrast. (B) Image acquired after 65 s, showing the formation of the liquid AuSi alloy as reflected by the rounded shapes in projection and the disappearance of crystalline contrast. (C) Image acquired after 84 s, showing the appearance of a Si nucleus with lighter contrast at the edge of one AuSi droplet. (D to F) Enlarged images of the boxed regions of (A) to (C), respectively. Arrows in (F) indicate the interface between liquid AuSi and solid Si.



<sup>1</sup>School of Materials Engineering and Birck Nanotechnology Center, Purdue University, West Lafayette, IN 47907, USA.

<sup>2</sup>IBM Research Division T. J. Watson Research Center, Yorktown Heights, NY 10598, USA.

\*Present address: Department of Materials Science and Engineering, University of California Los Angeles, Los Angeles, CA 90095, USA.

†To whom correspondence should be addressed. E-mail: eastach@purdue.edu (E.A.S.); fmross@us.ibm.com (F.M.R.)

Experiments were carried out in a UHV-TEM that is equipped with facilities for introducing the reactive gas disilane ( $\text{Si}_2\text{H}_6$ ) to a heated sample while it remains under observation (15–17). Nucleation and growth kinetics of Si were observed in nanoscale Au crystallites supported on an electron-transparent amorphous  $\text{SiN}_x$  membrane. Figure 1 shows a series of images as a function of disilane exposure time, showing the initial transformation of polycrystalline Au islands (Fig. 1A) into eutectic droplets of AuSi (Fig. 1B), followed by the appearance of Si nuclei (Fig. 1C). Enlargements in Fig. 1, D to F, show one reaction sequence in more detail, and movies S1 and S2 illustrate a complete video sequence and a magnified view of a single nucleation event. The general behavior is consistent with that reported in (10), but we took advantage of time-resolved measurements to focus on the kinetics of the initial nucleation. In all cases, we found that Si nucleation occurs at the edge of the droplet, which suggests that this is the energetically favorable location that minimizes the nucleation barrier (18). At later times, the Si nuclei grew into elongated wires. We did not analyze this stage of growth because of the random wire direction and geometry, but instead focused on the regime in which the nuclei are still small particles within the AuSi droplets.

Figure 2A shows a representative series of images of a Si nucleus after formation, and Fig. 2,

B and C, shows quantitative measurements of the radius  $r$  (defined in the figure caption) versus time  $t$  of this and several other nuclei obtained at 525°C from droplets of different volumes at two different pressures. The data show that after disilane was introduced at  $t = 0$ , a certain time elapsed (the incubation time) before the solid Si nucleus appeared. Each nucleus initially grew very rapidly but within a few seconds reached a crossover point (C), after which the growth slowed down. This crossover is visibly sharper at lower pressures, as seen by comparing Fig. 2, B and C. Larger droplets show a longer incubation time, as expected from scaling arguments (10, 19), and also show a larger initial jump in nucleus size.

To model these kinetics, we used the fact that disilane cracking on the droplet surface results in a steady supply of Si into the droplet, which causes the Si fraction within the droplet to increase continuously. This initially results in a transition from solid pure Au to a liquid AuSi alloy. As more Si is supplied, the mole fraction of Si in the AuSi liquid alloy increases. At thermodynamic equilibrium, solid Si would appear when the AuSi composition ( $c$ ) reaches the Si liquidus composition at the growth temperature ( $c_0$ ). However, for growth on a substrate different from Si, there is a nucleation barrier to form the new crystalline Si phase. As a result, the liquid becomes supersaturated with Si before nucleation. With increasing supersaturation, the nucleation barrier decreases, until solid Si finally nucleates and quickly captures most of the excess Si in the liquid in a rapid growth spurt (10). Subsequently, growth continues more slowly, at a rate determined by the steady external Si supply from the disilane vapor.

We explain this behavior with a simple kinetic model, in which the AuSi droplet and the

growing solid Si nucleus are each assumed to maintain a constant shape. The rate of Si addition to the droplet is proportional to  $PA$ , where  $A$  is the exposed surface area of the droplet and  $P$  is the nominal disilane pressure (19). The droplets were treated as independent, consistent with annealing experiments that show that surface diffusion of Au and Si on the substrate is not appreciable over the time of the experiment (20). Nucleation occurs at a time  $t_n$  when the composition is  $c_n (>c_0)$ . Once the solid nucleates, it grows rapidly, and we assumed that by the time it is large enough to be visible, the Gibbs-Thomson effect of interfacial curvature can be neglected. This means that the nucleus captures Si from the liquid at a rate proportional to  $c - c_0$  per unit area.

From these assumptions, we derived (17) the following equation for the evolution of the linear dimension  $r$  of the Si particle with time, valid when  $r$  is small as compared with  $R$ :

$$\frac{dr}{dt} = k_{LS} \left[ \alpha(c_n - c_0) + k_{VL} \frac{P}{R} (t - t_n) - \left( \frac{r}{R} \right)^3 \right] \quad (1)$$

with initial condition  $r = 0$  at  $t = t_n$ .  $R$  is the linear dimension of the AuSi droplet at the time of nucleation. The first term,  $c_n - c_0$  in Eq. 1, reflects the initial growth rate at  $t_n$ . The second and third terms ( $P/R$  and  $r^3/R^3$ ) represent the effect of  $c$  increasing because of Si addition from the vapor and decreasing because of Si capture by the nucleus. The three parameters controlling growth in Eq. 1 are the geometry-weighted supersaturation  $\alpha(c_n - c_0)$  and the vapor-liquid and liquid-solid rate constants  $k_{VL}$  and  $k_{LS}$ , respectively (which also include geometric factors); details are given in (17). The geometric factors cannot be

determined directly because we only have images of the droplets in projection.

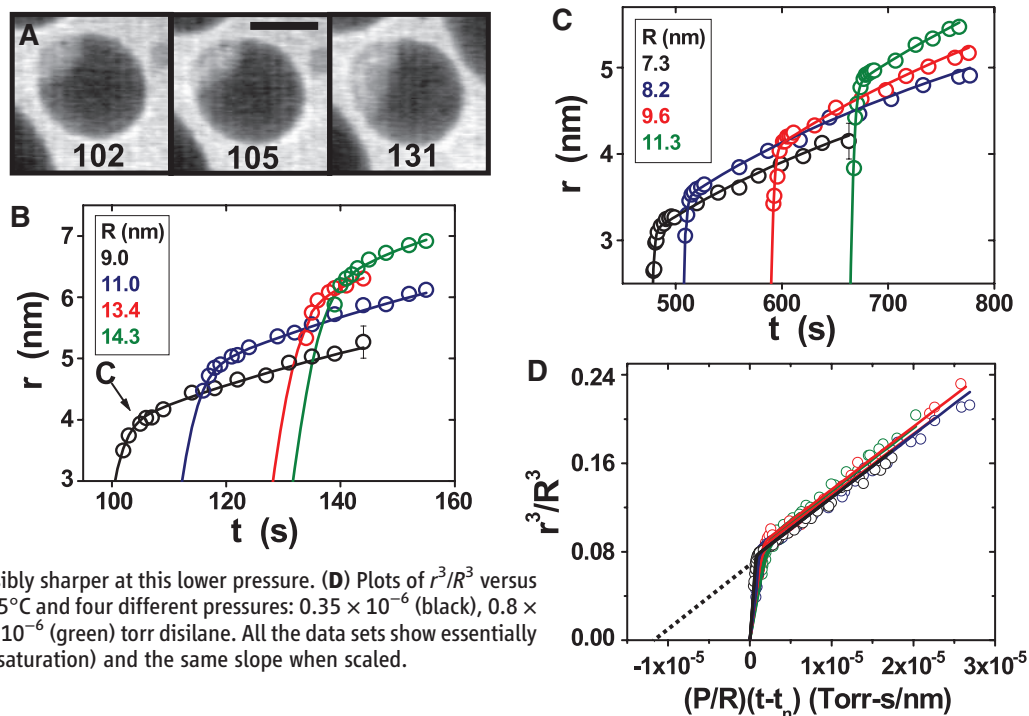
Although the assumptions are highly idealized, we found that Eq. 1 gives an excellent description of the data, as illustrated in Fig. 2. We measured 33 nucleation events with droplet radii ranging from 6 to 24 nm, temperatures from 470° to 585°C, and pressures from  $3.5 \times 10^{-7}$  to  $4.0 \times 10^{-6}$  torr. The complete set of data, and fits to Eq. 1, are shown in fig. S1. It can be seen that Eq. 1 automatically captures and quantifies our qualitative observations regarding the role of system size and growth rate. It predicts that larger droplets give later nucleation with larger jumps. It also predicts that the crossover is sharper at lower pressure, which is confirmed by examination of the complete set of data and fitted curves. We initially fitted each curve independently and confirmed that the resulting values for  $k_{LS}$  and  $k_{VL}$  were consistent for all droplets at a given temperature  $T$ , as expected. The values for the geometry-weighted supersaturation,  $\alpha(c_n - c_0)$ , were, surprisingly, also the same. We therefore fitted the entire data set for each  $T$  with a single value of each parameter. Figure 3 shows the fitted values of  $k_{LS}$ ,  $k_{VL}$ , and  $\alpha(c_n - c_0)$ .

The most dramatic aspect of the growth kinetics is the initial jump, which gives a direct visualization of the supersaturation as the nucleus captures the excess Si from the supersaturated liquid. Because the jump is quite sudden as compared with the incubation time and the subsequent slow growth, it is useful to consider Eq. 1 in the limit of large  $k_{LS}$ , giving

$$\frac{r^3}{R^3} \approx \alpha(c_n - c_0) + k_{VL} \frac{P}{R} (t - t_n) \quad (2)$$

In this limit, Si nucleates at  $t_n$  and “instantly” jumps to size  $r = [\alpha(c_n - c_0)]^{1/3} R$ . Subsequently,

**Fig. 2.** (A) Images of a growing Si nucleus acquired at the times specified, recorded during deposition at 525°C and  $4 \times 10^{-6}$  torr. Scale bar, 10 nm. (B) Linear dimension  $r$  of several Si nuclei versus time  $t$  for droplets of different initial radius  $R$  (as indicated in the box) during the same growth experiment. Approximating the nucleus image by an ellipse,  $r$  is calculated as the geometric mean of the semi-major and semi-minor axes; that is, the radius of a circle with an equivalent area. The “C” marks the crossover point (see text) of the data set from the droplet shown in (A); the middle image was recorded at this time. Solid curves are fits using Eq. 1. The error bar indicates measurement errors of ~5%. (C) Plots and fits of  $r$  versus  $t$  at  $T = 525^\circ\text{C}$  and  $P = 8 \times 10^{-7}$  torr. In comparison with (B), the crossover is visibly sharper at this lower pressure. (D) Plots of  $r^3/R^3$  versus  $(P/R)(t - t_n)$  for all nuclei analyzed at 525°C and four different pressures:  $0.35 \times 10^{-6}$  (black),  $0.8 \times 10^{-6}$  (blue),  $1.5 \times 10^{-6}$  (red), and  $4.0 \times 10^{-6}$  (green) torr disilane. All the data sets show essentially the same jump (that is, the same supersaturation) and the same slope when scaled.



its volume ( $\propto r^3$ ) grows linearly with time because of the steady supply of Si from the vapor phase. Equation 2 predicts that if we plot  $r^3/R^3$  versus  $(P/R)(t - t_n)$  for all the measurements at a given temperature, the data should collapse onto a single curve. This is confirmed in Fig. 2D for data obtained from different experiments at a fixed temperature of 525°C and covering a wide range of disilane pressures and droplet sizes. All the data sets show essentially the same jump (that is, the same supersaturation) and the same slope. This is an important test of the model and the assumptions underlying Eqs. 1 and 2. In particular, the collapse of the data onto a single curve confirms that there is no strong dependence of any of the model parameters, such as the shape factors, rate constants, and supersaturation, on  $P$  or on  $R$ , the system size.

Size effects in nucleation have been studied for decades. Until recently, the only observed size effects were attributed to defects or impurities

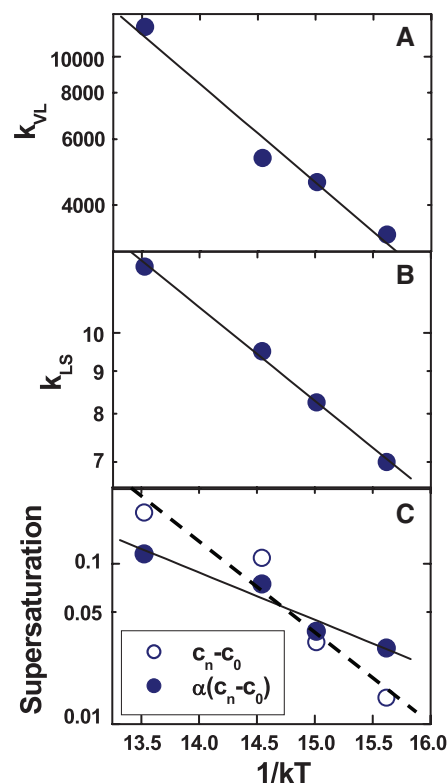


**Fig. 3.** (A to C) Parameter values versus temperature, shown on Arrhenius plots. These values are determined by fitting the entire data set shown in fig. S1, E to H. The solid and dashed lines are linear least-squares fits. (A) Vapor-liquid rate constant  $k_{VL}$ . (B) Liquid-solid rate constant  $k_{LS}$ . (C) Supersaturation at nucleation; solid circles indicate the parameter  $\alpha(c_n - c_0)$  obtained directly from the fitting of Eq. 1 and open circles indicate the absolute supersaturation  $c_n - c_0$  based on extrapolation from the growth kinetics after the jump. The two analyses exhibit a similar trend, in that the supersaturation at nucleation increases strongly with temperature.

(1, 3, 2I), although the possibility of intrinsic size effects due to the number of available sites was also considered (2I). The extrinsic size effects disappeared when the system was so small that it contained no impurities (1, 3, 2I). More recently, there have been reports of dramatic intrinsic size effects, with substantial changes in the fundamental phase diagram even for systems as large as 60 nm in diameter (5, 22–24). It therefore was surprising to find no effect in our own data, with diameters between 12 and 40 nm.

Thermodynamics predicts that the liquidus concentration  $c_0$  shifts by an amount roughly proportional to  $\gamma/R$ , whereas size effects on  $c_n$  are expected to be negligibly small by comparison (17). Here,  $\gamma$  involves geometrically weighted differences of the respective interfacial energies in the system, so it is highly system-dependent and has not to our knowledge been determined for any VLS system. Thus, we could not predict the magnitude of size effect expected, so we focused on the size scaling. For each temperature, our data span roughly a factor of 2 in size, so whatever size effects occur at our smallest size should be reduced by half at our largest size. Figure 2D shows that the scatter in jump height is very small; more quantitatively, we estimate that changes in  $\alpha(c_n - c_0)$  due to size are not more than 0.005 (0.5%), otherwise they would be observable as a systematic trend above the scatter. We therefore found a lack of sensitivity to size over the important range used to form nanowires for device applications, which is helpful for predictably engineering small structures.

Furthermore, we found that nucleation systematically occurs at the droplet edge, indicating that it is heterogeneous, with both surface and interface playing a role. This implies that the supersaturation needed for nucleation, and possibly even the extent of size effects, could be altered by appropriate pretreatment of the substrate. Yet the nucleation is intrinsic, being highly reproducible from drop to drop. Both facts are favorable for technological applications; reproducibility is essential for large-scale integration, and the role of the substrate in nucleation suggests opportunities for control via substrate engineering.

We now discuss the numerical values and physical importance of the fitted parameters. If we knew the three-dimensional shapes, and hence the geometric factors, the results in Fig. 3 would correspond to direct measurements of the two rate constants  $k_{VL}$  and  $k_{LS}$  and the critical supersaturation  $c_n - c_0$ . Even without this knowledge, we can determine the temperature dependences of the physical parameters if we assume that the shapes are independent of temperature. The kinetic rate constants are expected to be thermally activated, and indeed the measured values are consistent with this (Fig. 3). The slope for  $k_{VL}$  gives an activation energy of about 0.61 eV for the dissociative adsorption of disilane, in agreement with previous work (19).

The slope for  $k_{LS}$  gives an activation energy of about 0.26 eV for incorporation of Si from the AuSi liquid into the Si crystal. And the parameter  $\alpha(c_n - c_0)$  ranges from 3 to 12%, increasing with temperature.

The unknown geometrical factors are expected to be of order 1. But their presence causes uncertainty in extracting supersaturation from the parameter  $\alpha(c_n - c_0)$ . However, we can estimate the supersaturation without knowledge of the geometrical factors by using an entirely different approach (17). It relies on the assumption that the rate of addition of Si to the droplet is approximately constant over time and can be determined from the time to reach  $c_0$  (the  $x$  intercept of the dotted line in Fig. 2D). In Fig. 3C, we show values of supersaturation calculated using this approach. The results are similar to the results from the direct fitting, and the ratio (which ideally should be  $\alpha$ ) is of order 1, as expected for reasonable geometries. Both data sets in Fig. 3C show a similar trend with temperature. There is a difference in the slope, which could arise if the  $\alpha$  values depend on temperature (such as via the drop contact angle) or if there are other systematic deviations from our simplifying assumptions. In any case, two quite different approaches lead to the same conclusion, namely that the supersaturation at nucleation increases strongly with temperature.

The temperature dependence of the supersaturation is intriguing. We are not aware of prior results that explain this, and we can only speculate about the mechanism. The required supersaturation is controlled largely by the interfacial free energy of the Si nucleus (2), so the temperature dependence of  $c_n - c_0$  is likely to track the temperature dependence of this energy. The results are consistent with an Arrhenius behavior, with the smaller values at low temperature suggesting a reduced interface energy at low temperature. Temperature-dependent interface energies may be related to a temperature-dependent near-surface ordering that has recently been observed in AuSi (25) or to hydrogen coverage at the Si-vapor interface, which could depend on  $T$  via thermally activated disilane-cracking and H desorption.

We have shown detailed measurements of a nucleation and growth phenomenon, exploring the phase diagram of a nanoscale system at constant temperature and varying composition. The growth kinetics are explained by the buildup of a substantial supersaturation before nucleation. The lack of any change in supersaturation with system size suggests that the phase diagram has no appreciable size dependence in this system, at least down to  $\sim 12$  nm in diameter.

We believe that the results shown here are of fundamental interest in advancing the theoretical understanding of nucleation in nanoscale systems, a phenomenon that is of importance in materials design for nanotechnology and in crystal growth and phase transformations. The results are particularly relevant to the growth of nano-

wires from liquid eutectic droplets, the most common route of nanowire formation. A detailed understanding of nucleation and growth kinetics will help in engineering nanostructures for applications such as sensors, transistors, and logic circuits (26), in which size dependence, incubation times, and the reliability of nucleation itself must all be controlled for the successful fabrication of each nanoscale device.

#### References and Notes

1. D. Turnbull, R. E. Cech, *J. Appl. Phys.* **21**, 804 (1950).
2. D. Turnbull, J. C. Fisher, *J. Chem. Phys.* **17**, 71 (1949).
3. J. H. Perepezko, J. L. Sebright, P. G. Höckel, G. Wilde, *Mater. Sci. Eng. A* **326**, 144 (2002).
4. Y. Wu, P. Yang, *J. Am. Chem. Soc.* **123**, 3165 (2001).
5. P. W. Sutter, E. A. Sutter, *Nat. Mater.* **6**, 363 (2007).
6. B. Kalache, P. R. I. Cabarrocas, A. Fontcuberta i Morral, *Jpn. J. Appl. Phys.* **45**, L190 (2006).
7. T. Clement, S. Ingole, S. Ketharanathan, J. Drucker, S. T. Picraux, *Appl. Phys. Lett.* **89**, 163125 (2006).
8. K. C. Lu *et al.*, *Nano Lett.* **7**, 2389 (2007).
9. S. K. Eswaramoorthy, J. M. Howe, G. Muralidharan, *Science* **318**, 1437 (2007).
10. S. Hofmann *et al.*, *Nat. Mater.* **7**, 372 (2008).
11. R. S. Wagner, W. C. Ellis, *Appl. Phys. Lett.* **4**, 89 (1964).
12. C. Thelander *et al.*, *Mater. Today* **9**, 28 (2006).
13. V. Schmidt *et al.*, *Small* **2**, 85 (2006).
14. O. Hayden *et al.*, *Small* **3**, 230 (2007).
15. M. Hammar, F. K. LeGoues, J. Tersoff, M. C. Reuter, R. M. Tromp, *Surf. Sci.* **349**, 129 (1996).
16. F. M. Ross, J. Tersoff, M. C. Reuter, *Phys. Rev. Lett.* **95**, 146104 (2005).
17. Materials and methods are available as supporting material on Science Online.
18. R. P. Sear, *J. Phys. Condens. Matter* **19**, 033101 (2007).
19. S. Kodambaka, J. Tersoff, M. C. Reuter, F. M. Ross, *Phys. Rev. Lett.* **96**, 096105 (2006).
20. To establish this, we measured Au crystallite sizes and AuSi droplet sizes during annealing without growth. We did not observe appreciable changes in size, even for the smallest particles, which shows that Ostwald ripening need not be considered in these experiments.
21. T. Takahashi, W. A. Tiller, *Acta Metall.* **17**, 643 (1969).
22. J. G. Lee, H. Mori, *Phys. Rev. Lett.* **93**, 235501 (2004).
23. E. Sutter, P. Sutter, *Nano Lett.* **8**, 411 (2008).
24. H. Adhikari, A. F. Marshall, C. E. D. Chidsey, P. C. McIntyre, *Nano Lett.* **6**, 318 (2006).
25. O. G. Shpyrko *et al.*, *Science* **313**, 77 (2006).
26. W. Lu, C. M. Lieber, *J. Phys. D Appl. Phys.* **39**, R387 (2006).
27. We acknowledge A. Ellis and K. B. Reuter of IBM for their assistance with experimental aspects of this work, M. Comer of Purdue with assistance in image analysis, and financial assistance from NSF under grant DMR-0606395.

#### Supporting Online Material

www.sciencemag.org/cgi/content/full/322/5904/1070/DC1

Materials and Methods

Figs. S1 and S2

Movie S1 and S2

21 July 2008; accepted 17 October 2008

10.1126/science.1163494

# Spectroscopic Tracking of Structural Evolution in Ultrafast Stilbene Photoisomerization

Satoshi Takeuchi,<sup>1</sup> Sanford Ruhman,<sup>2</sup> Takao Tsuneda,<sup>3</sup> Mahito Chiba,<sup>4</sup> Tetsuya Taketsugu,<sup>5</sup> Tahei Tahara<sup>1\*</sup>

Understanding a chemical reaction ultimately requires the knowledge of how each atom in the reactants moves during product formation. Such knowledge is seldom complete and is often limited to an oversimplified reaction coordinate that neglects global motions across the molecular framework. To overcome this limit, we recorded transient impulsive Raman spectra during ultrafast photoisomerization of *cis*-stilbene in solution. The results demonstrate a gradual frequency shift of a low-frequency spectator vibration, reflecting changes in the restoring force along this coordinate throughout the isomerization. A high-level quantum-chemical calculation reproduces this feature and associates it with a continuous structural change leading to the twisted configuration. This combined spectroscopic and computational approach should be amenable to detailed reaction visualization in other photoisomerizing systems as well.

Molecular rearrangements in chemical reactions occur on a time scale comparable to nuclear vibrational periods (i.e., from 10 fs to 1 ps). This time scale is now accessible with advanced ultrafast vibrational spectroscopy (1), but, in almost all studies, we only observe structures in stationary (excited) states and the population transfer from one state to the other. Continuous changes of the molecular structure are seldom observed, especially for large polyatomic molecules. This situation often limits our understanding to a level of an oversimplified reaction coordinate (RC). To map

structural evolution and elucidate true RCs, it is crucial to track molecular vibrations during reactions, which characterize the global motions of the whole molecule. Recently, femtosecond infrared spectroscopy has provided highly time-resolved vibrational spectra, but the technique is practically limited to the  $>1000\text{ cm}^{-1}$  region (2). Conventional spontaneous Raman is only applicable to picosecond or slower processes, because long and narrow-band pulses are utilized to achieve sufficient frequency resolution ( $<15\text{ cm}^{-1}$ ). This drawback in time resolution was improved by the introduction of a stimulated Raman process with femtosecond pulses (3). With the use of this technique, geometric changes of the retinyl chromophore in visual pigments were uncovered by monitoring hydrogen out-of-plane wagging vibrations in the 800- to  $1000\text{-cm}^{-1}$  region (4). Common to these frequency-domain Raman approaches, however, is the challenge of observing low-frequency vibrations, given disturbance from strong Rayleigh scattering. Here we report a fem-

tosecond resonance Raman probing at the impulsive limit to follow the low-frequency spectral change accompanying structural evolution in a *cis*-*trans* photoisomerization in solution.

Femtosecond transient impulsive Raman spectroscopy is explained as a combined pump-probe and time-domain Raman technique using three laser pulses (5, 6), as shown in Fig. 1A (7). In this experiment, we first generate a reactive excited-state molecule by a pump pulse ( $P_1$ ). After a certain delay ( $\Delta T$ ), we introduce an ultrashort pulse ( $P_2$ ) resonant with the excited-state absorption and impulsively induce a vibrational coherence of Raman active modes, which is driven by two frequency components contained in the spectrum of the  $P_2$  pulse. In other words, the  $P_2$  pulse initiates the motion of a nuclear wave packet in the reactive excited state. The third pulse ( $P_3$ ) monitors the excited-state absorption, whose intensity is modulated by the nuclear wave-packet motion. Fourier transformation of the resultant beating feature in the time-resolved absorption provides a spectrum of the molecular vibration with a detectable range reaching into the low-frequency terahertz region, which is inaccessible by other frequency-domain methods. For long-lived stationary states, this time-domain measurement gives vibrational information equivalent to that obtainable from conventional frequency-domain Raman (8, 9). However, for structurally evolving states in a picosecond, this method can afford vibrational spectra with the best possible time- and frequency-resolutions that are determined only by the vibrational coherence time of the transients.

Stilbene is an extensively studied paradigm of ultrafast olefinic photoisomerization (Fig. 1B). In particular, *cis*-stilbene exhibits nearly barrierless bond twisting in the excited state that is complete within  $\sim 1\text{ ps}$  (10–15). The photoisomerization mechanism of *cis*-stilbene has been often discussed on the basis of a traditional one-dimensional (1D) potential energy surface (PES) along the torsional coordinate of the cen-

<sup>1</sup>Molecular Spectroscopy Laboratory, RIKEN, 2-1 Hirosawa, Wako 351-0198, Japan. <sup>2</sup>Institute of Chemistry, Hebrew University, Jerusalem 91904, Israel. <sup>3</sup>School of Engineering, University of Tokyo, Tokyo 113-8656, Japan. <sup>4</sup>National Institute of Advanced Industrial Science and Technology, Tsukuba 305-6568, Japan. <sup>5</sup>Graduate School of Science, Hokkaido University, Sapporo 060-0810, Japan.

\*To whom correspondence should be addressed. E-mail: tahei@riken.jp